

Rapid in-situ x-ray diffraction during the growth of ferroelectric superlattices

Benjamin Bein,¹ Hsiang-Chun Hsing,¹ Sara J Callori,^{1, a} John Sinsheimer,^{1, b}

Priya V. Chinta,² Randall L. Headrick,² and Matthew Dawber*¹

¹*Dept of Physics and Astronomy, Stony Brook*

University, Stony Brook, NY 11794-3800 USA

²*Department of Physics, Cook Physical Science Building,*

University of Vermont, Burlington, VT 05405 USA

Abstract

Ferroelectric domains, surface termination, average lattice parameter and bilayer thickness were monitored using in-situ synchrotron x-ray diffraction during the growth of BaTiO₃/SrTiO₃ (BTO/STO) superlattices by off-axis RF magnetron sputtering. A new x-ray diffraction technique was employed which allows for scan times substantially faster than the growth of a single layer of material, enabling continuous monitoring of multiple structural parameters as the film grows. Due to the large compressive strain experienced by the BTO layers in these substrates these superlattices are ferroelectric when grown and display continuous evolution of the polarization during growth. The effect of electric boundary conditions was investigated by growing the same superlattice alternatively on STO substrates and 20nm SrRuO₃ (SRO) thin films grown on STO substrates. The experiments provide insight into the formation and evolution of ferroelectric domains in the situation when the sample is ferroelectric during the growth process.

^a Now at: Bragg Institute, ANSTO, New Illawarra Road, Lucas Heights NSW 2234, Australia, and School of Physics, University of New South Wales, Sydney 2052, Australia.

^b Now at: Brookhaven National Laboratory, Upton, New York 11973-5000, USA.

* Email: matthew.dawber@stonybrook.edu

In ferroelectric thin films and multilayers, the polarization is intricately linked to crystal structure, so that strain and electrostatic boundary conditions have considerable impact on the magnitude of the polarization and the arrangement of polarization domains [1–5]. In certain strained ferroelectrics, for example BaTiO₃ (BTO) or PbTiO₃ (PTO) grown epitaxially on SrTiO₃ (STO), the ferroelectric transition temperature can lie above the growth temperature of the film [6], and thus the electrostatic boundary conditions may also be influential during the growth process. In-situ x-ray diffraction can provide an effective probe of structural parameters of ferroelectric thin films during growth without interfering with the ongoing process [4–8]. This study goes beyond thin films and considers the growth of artificially layered ferroelectric superlattices. During the growth of this class of artificial materials it is desirable to measure the out-of-plane lattice parameters, in-plane lattice parameters, the artificially created superlattice repeat periodicity and the spacing of ferroelectric domains. All of this information can be obtained by performing reciprocal space maps around appropriate Bragg reflections. Here we have developed a scanning technique that makes full use of the available x-ray intensity and area detector technology at X21 at the National Synchrotron Light Source (NSLS) at Brookhaven National Laboratory (BNL) to provide all of the desired information in substantially less time than it takes to deposit a single unit cell of material. This provides us with an unprecedented ability to monitor the continuous evolution of the polarization and related structural parameters during growth, elucidating the role of electrostatics and strain during the growth of ferroelectric superlattices.

Our experiments were performed in an in-situ growth chamber at the X21 beamline at NSLS. The chamber is configured as a 4-circle diffractometer with control over the ϕ, θ, δ and 2θ angles (see Fig. 1 (a), (d)). Two beryllium windows allow the x-ray beam to enter the chamber, scatter off the sample (which is heated to an appropriate temperature for deposition, in the present work, 650°C) and exit at the position of the detector, which is a PILATUS-100K area detector. Fig. 1 (a), (d) shows a schematic of the experimental setup for scans in the vicinity of the (001) and (101) peaks of the substrate. Two shuttered magnetron sources, mounted in an off-axis geometry, enabled the deposition of BTO and STO. Superlattices composed of alternating layers of BTO and STO have been intensively studied in theory and experiment [9–17].

To calibrate the growth rates of STO and BTO the intensity of the reflected signal at the (00 $\frac{1}{2}$) Bragg position (to minimize bulk Bragg diffraction) [8, 19, 20]) was measured as a

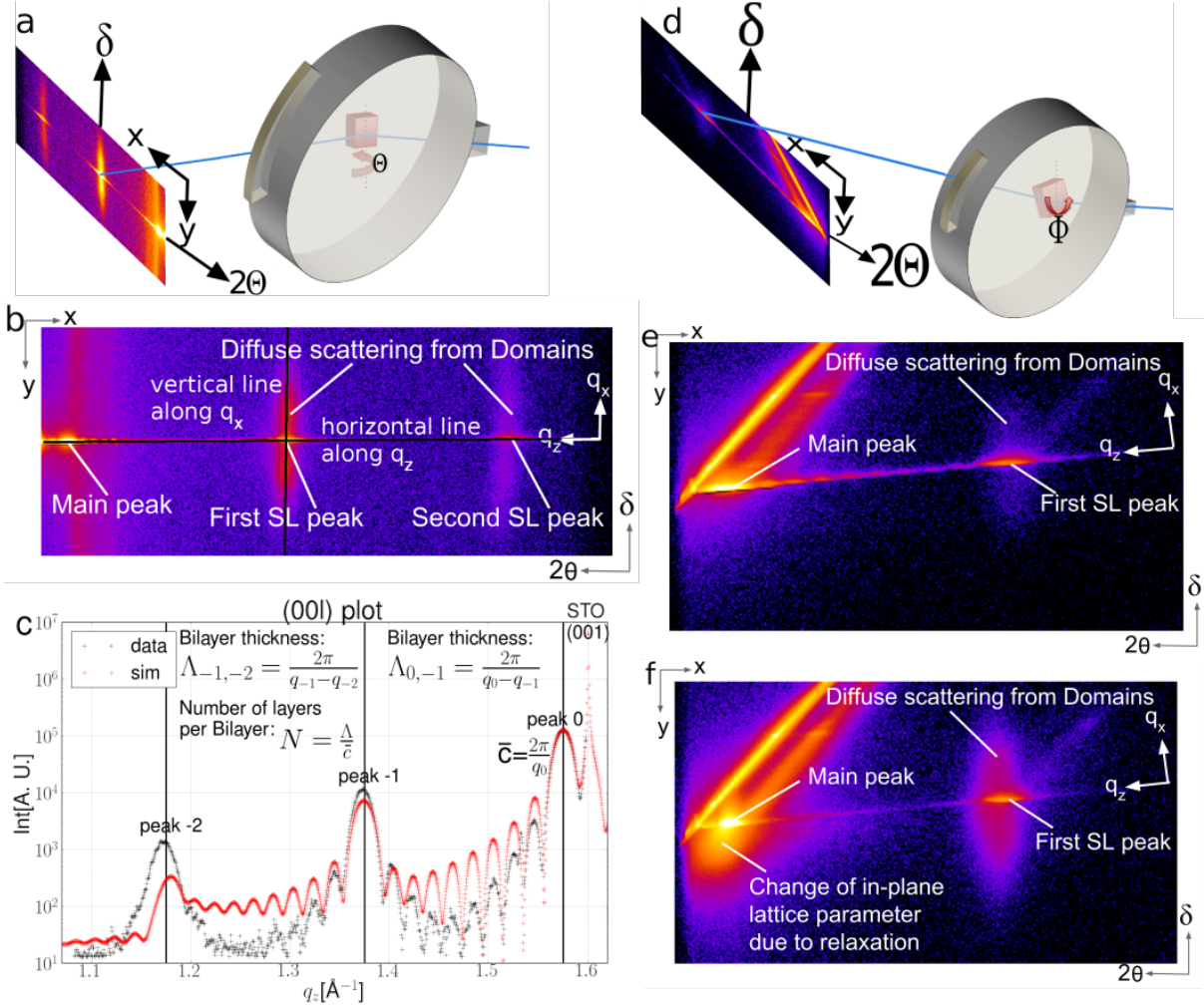


FIG. 1. Experimental setup: (a) A schematic of the experimental setup illustrating the angles used for (001) scans, (b) a single exposure of the Pilatus detector during our experiment with the corresponding detector, diffractometer and momentum transfer axis, (c) example data (black) along (001) direction after the growth of 10 bilayers together with a fit (Red). Basic superlattice attributes are also illustrated. (d) A schematic of the experimental setup illustrating the angles used for (101) scans, (e) image of a single scan around (101) after 10 bilayers is shown with the corresponding detector, diffractometer and momentum transfer axis, (f) image of a single scan around (101) after 30 bilayers with the corresponding detector, diffractometer and momentum transfer axis.

function of time. The intensity of the reflectivity signal provides a measurement of surface roughness. Oscillations in this intensity can be followed in a similar manner to reflection high energy electron diffraction (RHEED) oscillations [18], though the RHEED technique is not appropriate for use with magnetron sputtering (due to the magnetic fields present) and does not provide the same amount of structural information as x-ray diffraction can. In the case of layer by layer growth, the maxima in the reflectivity intensity correspond to completed layers while low reflectivity signals correspond to incomplete layers.

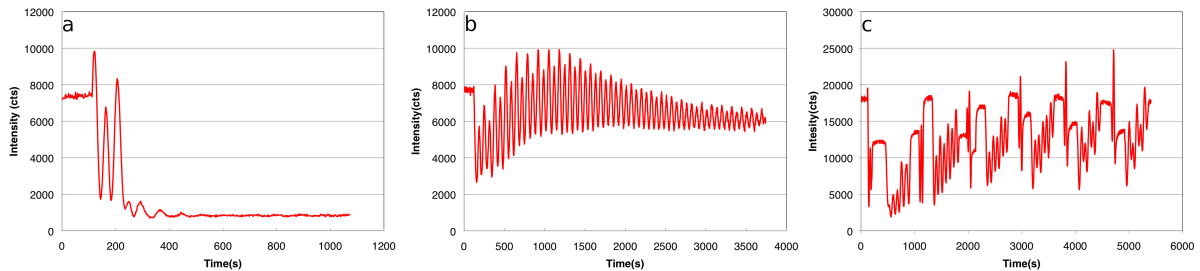


FIG. 2. Reflectivity: (a) reflectivity scan of BTO on STO, (b) STO grown on STO and (c) BTO/STO 2/6 superlattice grown on STO. It can be seen that the BTO stops growing in a smooth way after two layers. The STO on the other hand continues to grow smoothly in a layer-by-layer mode for many layers. The BTO/STO superlattice continues to show intensity oscillations for each BTO double layer. STO layers in the superlattice help maintain the BTO growth in a smooth layer by layer mode.

Fig. 2 shows reflectivity data for BTO(a), STO(b) and a BTO/STO superlattice(c). BTO stops growing with well defined intensity oscillations after two layers, while for STO oscillations can be observed for many layers. In a superlattice with bilayers consisting of 2 unit cell layers of BTO and 6 unit cell layers of STO on top of the BTO (2/6 BTO/STO), BTO and STO have intensity oscillations for multiple superlattice bilayers. This allows the growth of a larger total number of BTO layers than in a coherently strained thin film of BTO on STO before the intensity oscillations are no longer observable. Intensity oscillations most likely disappear because of a misfit strain induced change in growth mode from layer by layer growth to island growth. Precise growth rates for the materials are presented in supplementary information (A).

Once growth rates had been determined, we investigated the evolution of structural prop-

erties related to electrical polarization in ferroelectric superlattices, based on the comparison of the growth of two compositions of BTO/STO superlattices grown with different electrical boundary conditions. The compositions chosen were 2/6 BTO/STO and 1/7 BTO/STO. The reason for choosing these compositions were that the reflectivity measurements showed us that the thin BTO layers within these superlattices could be expected to maintain high quality, while the overall superlattice periodicity of 8 unit cells led to ideal positioning of the superlattice peaks on the Pilatus detector. Two samples of each composition were grown, one on a bare STO substrate and the other on top of a ~ 20 nm SRO film, which provided a conductive boundary condition to the bottom of the sample. The in-plane lattice parameters of the SRO films were constrained to that of the STO substrate.

To be able to rapidly acquire an extensive set of structural parameters during growth a new scanning technique, akin to a time-resolved rotating crystal method [21], was employed. One motor was moved continuously through a given angular range while the Pilatus detector integrated all the intensity which reached it during the motion of that motor. Because of the high quality of the film and substrate they both have a sharp rocking curve peak, so the diffraction condition is only met in a very narrow angular range of the scanned motor for each 2θ angle. The respective motor movement in each scan corresponds to the movement normally performed during a rocking curve. Therefore the measured intensity of each pixel is the integrated intensity over the rocking curve at that pixel. This leads to integration over one in-plane reciprocal space direction (k) while diffraction information in the two other reciprocal space directions (h and l) can be obtained from each camera image. This technique can be employed for the (001) reflection by scanning the θ motor (Fig. 1(a)), and for the (101) reflection by scanning the ϕ motor (Fig. 1(d)). Some further explanation of the method is given in supplementary information B and supplementary figure S1.

An example of the (001) data obtained is shown in Fig. 1(b). The obtained images can be assembled into continuous movies which allow the observation of the evolution of diffraction features during the growth (See supplementary information E and movie files). Our analysis of the data contained in these images is based on two principle lines of points. The first line is along the Q_z direction which is a horizontal line in Fig. 1(b). A plot along this line together with a fit to the data and basic superlattice attributes are shown in Fig. 1(c). The second line of interest in Fig. 1(b) is a vertical line through the first superlattice diffraction peak. It is along the Q_x direction and gives information about the polarization

domain periodicity in the superlattice.

Much can be learned about the superlattice from the data on the horizontal line along (001). For instance, the position of the main, first and second superlattice peak can be tracked during the growth. The average out of plane lattice parameter \bar{c} , can be approximated from the measured position of the main superlattice peak [22] and the result is shown in Fig. 3 (a). This measurement is reliable after the superlattice has a total thickness of 30nm, or in this case, 10 bilayers. Until that thickness is reached the superlattice peak intensity is weak compared to the tail of the substrate peak, which affects the apparent value of the lattice parameter of the film. On samples with a SRO bottom electrode interference with the diffraction from the thin film electrode makes it even harder to determine \bar{c} accurately by direct measurement of the film peak intensity. As we discuss later, fitting the data using kinematic x-ray theory can overcome these problems.

From the positions of the main and first superlattice peak one can measure the number of unit cell layers per bilayer N (Fig. 3 (b)). This figure shows that the grown superlattice has ~ 7.9 unit cells per bilayer, which is close to the desired 8 unit cell layers per bilayer. By tracking the first and second superlattice peak intensity the quality of the superlattice can be monitored. A high quality superlattice will have an increasing peak intensity with increasing thickness, while the intensity will be reduced if the superlattice loses its high quality. Fig. 3 (c) and (d) shows plots of the first and second superlattice peak intensities against the superlattice thickness. The data shows that samples grown on SRO bottom electrodes maintain their excellent quality during the whole growth up to 100nm, while samples grown on plain STO substrates start losing superlattice peak intensity after 30nm. The most likely cause of this change in intensity is in-plane relaxation of the superlattice, which is illustrated in Fig. 1 (e) and (f). In Fig. 1 (e) an image from a single scan around (101) after 10 bilayers is shown with the corresponding detector, diffractometer and momentum transfer axis and Fig. 1 (f) shows the corresponding image after 30 bilayers. The new feature below the main superlattice peak after 30 bilayers that does not exist in the scan after 10 bilayers is explained by relaxation of the in-plane lattice parameters in the thicker superlattice.

To extract reliable values of structural parameters from the experimental data, appropriate fitting approaches (described in Methods) had to be applied. This is particularly important for very thin films or superlattices with a small number of bilayers, where inter-

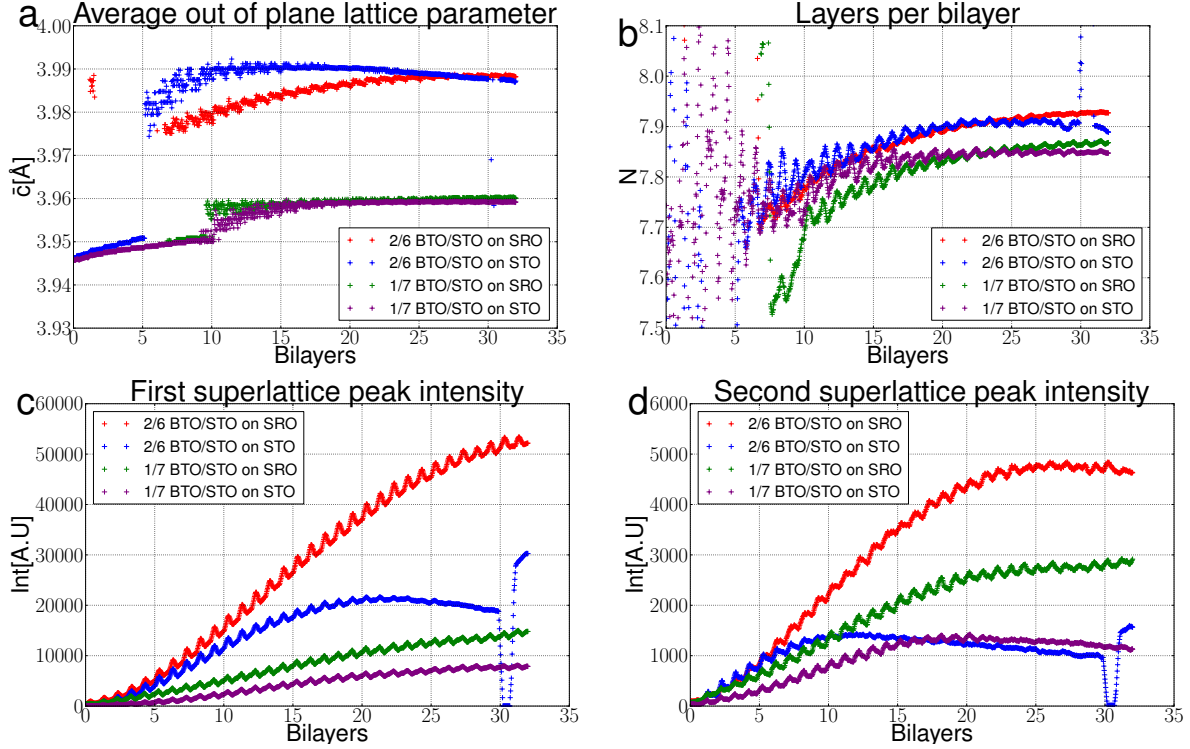


FIG. 3. Evolution of peak intensities: The figure shows (a) \bar{c} , (b) N , (c) first and (d) second superlattice peak intensity plotted vs the number of bilayers. From, (b), the plot of the number of unit cell layers per bilayer, N , it can be seen that the superlattices are grown close to the desired 8 unit cell layers per bilayer. The earlier reduction of the superlattice quality of the samples grown on plain STO can be seen in the decay of the first and second superlattice peak intensities (plots (c) and (d)) as well as in the reduction of \bar{c} with increasing thickness in (a). A larger \bar{c} for the 2/6 BTO/STO than the 1/7 BTO/STO superlattice is also seen in (a), arising from the larger volume fraction of BTO.

ference between the substrate and the deposited materials can shift the maximum of the peaks close to the substrate. By fitting model parameters so that the calculated diffraction patterns match the measurements one can extract the desired information even for very thin films.

It became apparent from the fitting that the termination of our superlattices changes during the growth process. By comparing different simulated terminations with the experimental data (See supplementary information C and supplementary figure S2) we found that after one bilayer was deposited, the fits to the diffraction data indicated the STO layers had

a SrO termination and the BTO layers had BaO termination. This is interesting considering that the initial termination of the substrates was known to be TiO_2 . First principles calculations do indicate that the BaO termination is energetically more favorable than TiO_2 in ultra-thin BTO thin films at this strain condition [23], which may be the driving force for this change of termination in the superlattice.

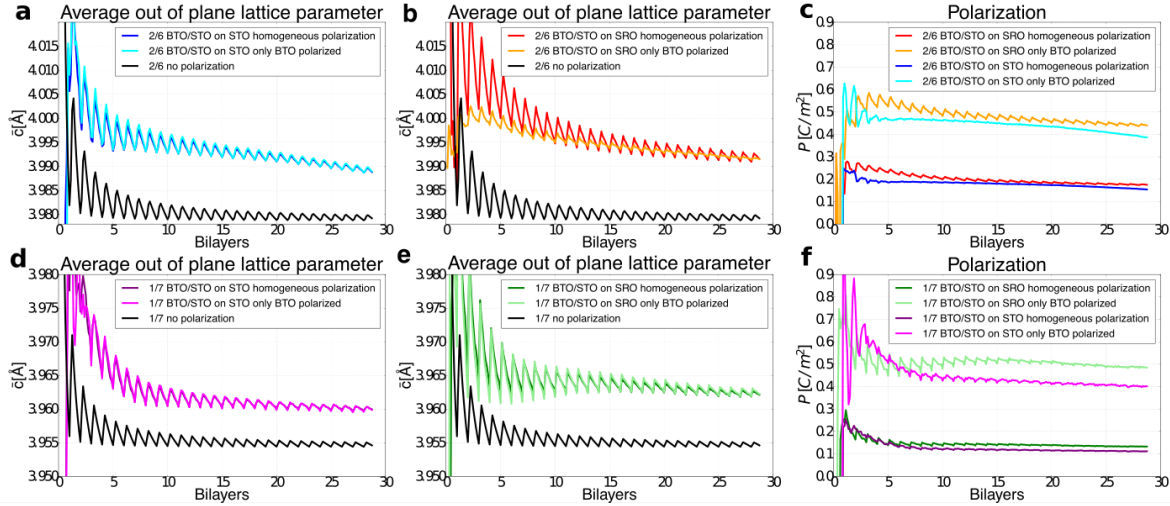


FIG. 4. Evolution of fitted \bar{c} and polarization: Fitted \bar{c} values for the (a) 2/6 BTO/STO sample grown on STO, (b) 2/6 BTO/STO sample grown on SRO, (d) 1/7 BTO/STO sample grown on STO, (e) 1/7 BTO/STO sample grown on SRO together with expectations from elastic theory (black curves) for non-polar samples. Like the raw data, the fits show that samples grown on SRO have a larger value for \bar{c} which is explained by a larger polarization within the elastic theory. The corresponding polarization for the two limiting models (the homogenous polarization scenario in which BTO and STO carry the same polarization and the scenario only BTO is polarized) are shown in (c) for the 2/6 BTO/STO superlattices and (f) for the for the 1/7 BTO/STO superlattices. The difference of the 2/6 BTO/STO superlattices from the elastic theory value is more than twice as big as that of the 1/7 BTO/STO samples, implying that the out of plane polarization of the 2/6 BTO/STO samples is larger than in the 1/7 BTO/STO samples.

Known elastic constants for BTO [25] and STO [26] were used to calculate the expected value for \bar{c} in the absence of polarization (black curve) and compare it with our fitted values in Fig. 4 (a), (b), (d), (e). It is obvious that the measured values are higher than a paraelectric sample would display. This is explained by the existence of ferroelectric

polarization, which is coupled to \bar{c} [3, 22]. Furthermore \bar{c} is larger for the samples grown on a SRO bottom electrode, suggesting that a superlattice grown on a SRO bottom electrode is more polar. After the samples had been cooled and removed from the growth chamber piezo force microscopy (PFM) (shown in supplementary information D and supplementary figure S3) was successfully performed on the samples to confirm that they are indeed ferroelectric.

Some care needs to be taken with the use of elastic constants and lattice parameters for stoichiometric materials in this kind of analysis. For example, when Zubko et al [27], investigated the lattice parameters of PTO/STO superlattices at room temperature, they used a STO lattice parameter of 3.92\AA , rather than the typical value of 3.905\AA . This increased lattice parameter was justified based on measurements of a STO thin film and is associated with imperfect stoichiometry of the STO film [28]. However, in the case of our experiments, when a $\theta - 2\theta$ scan around the (001) substrate peak for the STO film grown in Fig.2 (b) was performed immediately after the growth had finished it was nearly indistinguishable from that performed on the substrate before deposition. Our growth parameters are somewhat different from those used by Zubko et al. [27], who used a pressure of 0.18 Torr and a temperature of 520°C , compared to the pressure of 0.025 Torr and 650°C that we used.

Two limiting cases are considered for the possible distribution of polarization between the layers in the superlattice. The first case is extremely strong coupling between layers, leading to a *homogeneous polarization model*. In this model polarization can be considered homogeneous throughout the superlattice, with both materials (BTO and STO) having the same polarization value [13, 29]. This results in a polar dependence for both $c_{BTO}(P)$ and $c_{STO}(P)$, according to conventional strain polarisation coupling relationships. In the other extreme, in which layers are essentially decoupled, the ferroelectric material, BTO, is polarized and the dielectric material, STO, has no polarization, ie. an *only BTO polarized model*. This time only $c_{BTO}(P)$ depends on the polarization and c_{STO} is independent of the polarization. Most likely, the actual distribution of polarization will be somewhere between these two extremes [30]. For both of these models, the polarization value was used as a fitting parameter to produce the lattice parameters that go into the x-ray diffraction equations, and varied to obtain the best fit to the experimental diffraction pattern. Following this, \bar{c} is extracted from the lattice parameters which produced the best fit. The results are shown in Fig. 4 (a), (b), (d), (e).

Our measured values can be compared with simple calculations we performed based on

the thermodynamic potential of Li et al. [24], which was found to perform well for BTO grown on DyScO₃ and GdScO₃ [25]. The cubic lattice parameter of bulk BTO single crystal at 650°C is 4.025 Å (measured by Choi et al. [25]) while that of STO (measured directly in this experiment) is 3.93 Å. The mismatch strain at the growth temperature for BTO on STO is therefore -2.3%. The thermodynamic potential of Li et al. predicts that BTO at this strain and temperature should be ferroelectric, with a polarization of 0.24 C/m². This value is much closer to that of the *homogeneous polarization model* ($P \sim 0.2 \text{ C/m}^2$). For the *only BTO polarized model* the values of polarization ($P \sim 0.45 \text{ C/m}^2$) are implausibly high. The development of polarization during the growth for both models is shown in Fig. 4 (c) and (f). One interesting observation is that, independent of which model is used, for samples grown on SRO the polarization has a more pronounced sawtooth like oscillation of the polarization as each BTO layer is deposited the polarization increases a little and then it decreases again as the next STO layer is deposited.

Another indication of ferroelectric polarization is diffuse scattering along the vertical line (Q_x direction) through the first superlattice peak in Fig. 1 (b). This is a sign of periodic in-plane features, which are typically associated with a polarization stripe domain structure in ferroelectric materials. Fig. 5 (a) shows the diffuse scattering together with the fit to the data. To analyze the diffuse scattering we assumed a gaussian distribution of the stripe domain size and a Lorentzian intensity distribution for the superlattice peak. The position of the fitted gaussian is the average domain size of the superlattice and is plotted against the total superlattice thickness in Fig. 5 (c). To highlight the shape of the diffuse scattering and its change with increasing superlattice thickness, the data was rescaled in Fig. 5 (b). The rescaling was done by dividing the data by the the peak diffuse scattering intensity from the fit. The early stage (after 7 bilayers) and the late stage (after 25 bilayers) of the 2/6 BTO/STO superlattice grown on STO are compared in Fig. 5 (b). This comparison reveals that domain size remains fairly constant despite the thickness of the the film changing substantially, which we saw consistently for all of the superlattices (see Fig. 5 (c)).

The \bar{c} measurements suggest that polarization is rather homogeneous with similar values of polarization in the BTO and STO layers. In this scenario it might be expected that the domain size evolves during growth according to the Kittel Law [31], which predicts that the domain wall period should scale as $t^{\frac{1}{2}}$, as the thickness of the film, t , increases. Such behaviour is not observed, but it is noticeable that the domains are substantially

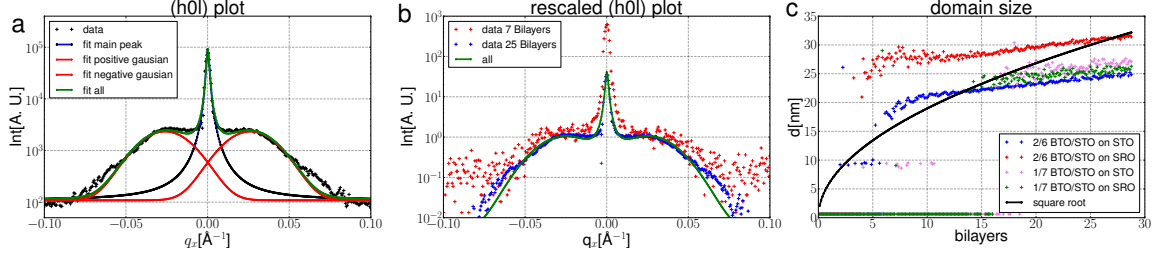


FIG. 5. Domains: (a) A plot through the diffuse scattering region together with a fit (green line) to the data. To fit the diffuse scattering we assumed a Gaussian distribution of domain sizes, these are illustrated in red. For the main peak we used a Lorentzian distribution which is shown in blue. (b) Data from early in the growth (after 7 bilayers) and later (after 25 bilayers) was rescaled by dividing it by the peak diffuse scattering intensity of the fit. (c) The average domain size plotted against the sample thickness. One can see that the square root relationship between domain size and film thickness typically expected for ferroelectric systems does not describe our data well.

bigger for the 2/6 BTO/STO sample grown on SRO, which aligns with the expectation that the screening provided by a metallic bottom electrode should reduce the need for domain formation. In experiments on PTO thin films where scaling of domain size with thickness was observed [4], the domains form once a film of a given thickness has been grown in the paraelectric phase and subsequently cooled. By contrast, in our experiments, domains form at some point in the growth process and the film thickness continues to increase after this has occurred. Our results suggest that domain size becomes “locked” very early in the growth of the superlattice, and so while electrostatic boundary conditions influence domains in the very early stages of growth they do not change very much after that. A locked domain period does not imply that the polarization state of the superlattice is fixed [32–35], and the oscillations we observe in the polarization required to fit the structural data would suggest that the polarization is actually in a continuous state of evolution as the film grows.

An increase in domain size requires domain walls to annihilate so that larger domains can be created and although the system would benefit energetically from an increase in domain size, there needs to be sufficient thermal motion of domain walls for annihilation events to take place, and this does not appear to occur here. Paruch et al. [36, 37] observed that thermal roughening of domain walls in PZT thin films is on the order of 1-2 nm in the temperature region used for growth in these experiments, well below the measured

domain sizes here ($\sim 20\text{-}30$ nm) and 90° domain walls in bulk BTO also seem to be stable against temperature induced annihilation until very close to the ferroelectric-paraelectric phase transition [38–40]. Our finding that domain size in ferroelectric superlattices can be influenced by electrostatic boundary conditions during growth and locked in early in the deposition process can provide a route for engineered domain sizes precisely targeted towards particular applications [41].

METHODS

A. Experimental Methods

The experiments presented here were performed at the NSLS beam line X21 using an x-ray energy of 10keV. The experiments were performed in an in-situ growth chamber with temperature, pressure and atmospheric control. The chamber is configured as a 4-circle diffractometer with control over the ϕ, θ, δ and 2θ angles (see Fig. 1 (a) and (d)). Two beryllium windows allow the x-ray beam to enter the chamber, scatter off the sample and exit at the position of the detector, a PILATUS-100K area detector. All films and superlattices grown in this experiment were grown by off-axis magnetron sputtering and under the same growth conditions. The pressure was kept at 0.025 Torr with an oxygen/argon ratio of 7:16. The growth temperature was 650°C . The RF power applied to the magnetron sources was 30W.

The materials that were deposited in the chamber in these experiments were BTO and STO. In all experiments high quality STO substrates from CrysTec GmbH with miscut angles $\sim 0.15^\circ$ and single unit cell steps of $\sim 0.4\text{nm}$ were used. The substrates had been etched in buffered HF and annealed by the vendor to ensure a TiO_2 surface termination. Some experiments were performed with deposition directly on to the STO substrates, which provides an insulating boundary condition. When this was done the substrates were annealed for 20 min at 750°C in a 0.05mTorr oxygen atmosphere directly prior to deposition to improve the quality of the surface. Other experiments were performed with deposition onto SRO bottom electrodes to provide a conductive boundary condition. The SRO films used were 20nm thick and grown prior to the in-situ experiments in an off-axis magnetron sputtering chamber at Stony Brook University. The SRO films were also atomically flat with single

unit cell steps of 0.4nm, and it was verified by x-ray diffraction prior to deposition that these films were epitaxially constrained to the STO substrate and had the same in-plane lattice parameter as the substrates.

B. Fitting methods

The starting point of the fitting is the diffraction equation:

$$I \propto A^2, A \propto \sum_{\vec{r}} f_{\vec{r}}(\vec{Q}) \cdot \exp(-i\vec{Q} \cdot \vec{r}) \quad (1)$$

where \vec{r} is the position of one atom and the sum runs over all atoms in the structure. \vec{Q} is the momentum transfer during the scattering and $f_{\vec{r}}(\vec{Q})$ is the atomic scattering factor, where \vec{r} denotes that there might be different atoms at different positions.

In this paper the (001) crystal truncation rod is investigated with quantitative fits so that for the fits only Q_z is non 0. In this case the diffraction amplitude from a thin film of N unit cells can be approximated by:

$$A \propto \sum_{n=0}^N F(\vec{Q}) \cdot \exp(-i \cdot Q_z \cdot c \cdot n - \epsilon \cdot n) = \frac{\exp(-i \cdot Q_z \cdot c \cdot N - \epsilon \cdot N)}{1 - \exp(-i \cdot Q_z \cdot c - \epsilon)} \quad (2)$$

where $F(\vec{Q})$ is the structure factor, ϵ is the absorption coefficient and c is the out of plane lattice parameter. To calculate the diffraction pattern of the superlattice one needs to add up the diffraction amplitude from all films and multiply it by the phaseshift to the surface of the sample. For the whole superlattice this leads to:

$$\begin{aligned} A_{total} &= A_{sub} \cdot \exp(-i \cdot Q_z \cdot (t_{el} + t_{super})) + \\ &A_{el} \cdot \exp(-i \cdot Q_z \cdot t_{super}) + \\ &A_{super} \end{aligned} \quad (3)$$

$$A_{super} = \sum_{l=0}^{N_{SL}} (A_{STO} + A_{BTO} \cdot \exp(-i \cdot Q_z \cdot t_{STO})) \cdot \exp(-i \cdot Q_z \cdot (t_{STO} + t_{BTO}) \cdot l)$$

with $t_{electrode}, t_{superlattice}$ as the total thickness of the electrode, superlattice respectively and N_{SL} is the number of bilayers in the superlattice. t_{STO}, t_{BTO} are the thickness of the BTO/STO layer in one bilayer. A standard gaussian surface roughness term of $\exp(-\sigma^2 \cdot (Q_z - Q_{001})^2)$ was used with σ as the rms roughness of the surface. Non integer film thicknesses are achieved by averaging over integer films.

ACKNOWLEDGMENTS

This work was supported by NSF DMR1055413. Development of the in-situ growth facility used in this work was supported by NSF DMR0959486. PVC and RLH were supported by U.S. Department of Energy, Office of Science, Office of Basic Energy Sciences, under Contract No. DE-FG02-07ER46380. A. DeMasi, M.H. Yusuf, H. Yusuf, J.G Ulbrandt, S. LaMarra and C. Nelson are thanked for their assistance with the experimental work. Use of the National Synchrotron Light Source, Brookhaven National Laboratory, was supported by the U.S. Department of Energy, Office of Science, Office of Basic Energy Sciences, under Contract No. DE-AC02-98CH10886. MD acknowledges support from the Donostia International Physics Center (DIPC) and CIC Nanogune which enabled helpful discussions with P. Aguado-Puente and E. Artacho.

AUTHOR CONTRIBUTIONS

All authors participated in the experimental work at NSLS. BB was chiefly responsible for the subsequent processing and analysis of the data. The experimental apparatus was designed, assembled and integrated in to the X21 beamline by JS, RLH and MD. MD devised the new experimental methods and directed the project. The manuscript was prepared by BB and MD with contributions from the other authors.

-
- [1] Junquera, J. & Ghosez, P. Critical thickness for ferroelectricity in perovskite ultrathin films. *Nature* **422** 506 (2003).
 - [2] Dawber, M., Chandra, P., Littlewood, P.B. & Scott, J.F. Depolarization corrections to the coercive field in thin-film ferroelectrics. *J. Phys. Condens. Mater.* **15** L393 (2003).

- [3] Lichtensteiger, C., Triscone, J.-M., Junquera, J. & Ghosez, P. Ferroelectricity and tetragonality in ultrathin PbTiO_3 films. *Phys. Rev. Lett* **94** 047603 (2005).
- [4] Streiffer, S.K. et al. Observation of nanoscale 180 degrees stripe domains in ferroelectric PbTiO_3 thin films. *Phys. Rev. Lett* **89** 067601 (2002).
- [5] Fong, D.D. et al. Ferroelectricity in ultrathin perovskite films. *Science* **304** 1650 (2004).
- [6] Sinsheimer, J. et al. In-situ x-ray diffraction study of the growth of highly strained epitaxial BaTiO_3 thin films. *Appl. Phys. Lett.* **103** 242904 (2013).
- [7] Fong, D.D. & Thompson, C. In Situ Synchrotron x-ray studies of ferroelectric thin films. *Annu. Rev. Mater. Res.* **36** 431 (2006).
- [8] Chinta, P.V., Callori, S.J., Dawber, M., Ashrafi, A. & Headrick, R.L. Transition from laminar to three-dimensional growth mode in pulsed laser deposited BiFeO_3 film on (001) SrTiO_3 . *Appl. Phys. Lett.* **101** 201602 (2012).
- [9] Tabata, H., Tanaka, H. & Kawai, T. Formation of artificial $\text{BaTiO}_3/\text{SrTiO}_3$ superlattices using pulsed-laser deposition and their dielectric-properties. *Appl. Phys. Lett.* **65** 1970 (1994).
- [10] Ishibashi, Y., Ohashi, N., and Tsurumi, T. Structural refinement of X-ray diffraction profile for artificial superlattices. *Jap. J. Appl. Phys.* **39** 186 (2000).
- [11] Nakagawara, O., Shimuta, T. & Makino, T. Epitaxial growth and dielectric properties of (111) oriented $\text{BaTiO}_3/\text{SrTiO}_3$ superlattices by pulsed-laser deposition. *Appl. Phys. Lett.* **77** 3257 (2000).
- [12] Shimuta, T., Nakagawara, O. & Makino, T. Enhancement of remanent polarization in epitaxial $\text{BaTiO}_3/\text{SrTiO}_3$ superlattices with "asymmetric" structure. *Jap. J. Appl. Phys.* **91** 2290 (2002).
- [13] Neaton, J.B. & Rabe, K.M. Epitaxial BiFeO_3 multiferroic thin film heterostructures. *Appl. Phys. Lett.* **82** 1586 (2003).
- [14] Johnston, K., Huang, X., Neaton, J.B. & Rabe, K.M. First-principles study of symmetry lowering and polarization in $\text{BaTiO}_3/\text{SrTiO}_3$ superlattices with in-plane expansion. *Phys. Rev. B* **71** 100103(R) (2005).
- [15] Jiang, A.Q., Scott, J.F., Lu, H.B. & Chen, Z.H. Phase transitions and polarizations in epitaxial $\text{BaTiO}_3/\text{SrTiO}_3$ superlattices studied by second-harmonic generation. *J. Appl. Phys.* **93** 1180 (2003).

- [16] Rios, S. et al. Orthorhombic strontium titanate in BaTiO₃-SrTiO₃ superlattices. *J. Phys. Cond. Matt.* **15** 305 (2003).
- [17] Kathan-Galipeau, K. et al. Quantification of Internal Electric Fields and Local Polarization in Ferroelectric Superlattices. *ACS Nano* **5** 640 (2011).
- [18] Rijnders, G.J.H.M, Koster, G. Blank, D.H.A & Rogalia H. In situ monitoring during pulsed laser deposition of complex oxides using reflection high energy electron diffraction under high oxygen pressure. *Appl. Phys. Lett* **70** 1888 (1997).
- [19] Vlieg, E. et al., Surface X-ray scattering during Crystal Growth: Ge on Ge(111). *Phys. Rev. Lett.* **61** 2241 (1988).
- [20] Ramana Murty, M. V. et al. In situ x-ray scattering study of PbTiO₃ chemical-vapor deposition. *Appl. Phys. Lett.* **80** 1809 (2002).
- [21] Warren, B.E.. X-ray diffraction. (Dover Publications, Inc., New York, 1990).
- [22] Dawber, M. et al. Unusual behavior of the ferroelectric polarization in PbTiO₃/SrTiO₃ superlattices. *Phys. Rev. Lett* **95** 177601 (2005).
- [23] Dionot, J., Geneste, G., Mathieu, C. & Barrett, N. Surface polarization, rumpling, and domain ordering of strained ultrathin BaTiO₃(001) films with in-plane and out-of-plane polarization. *Phys. Rev. B* **90** 014107 (2014).
- [24] Li, Y.L., Cross, L.E. & Chen L.Q. A phenomenological thermodynamic potential for BaTiO₃ single crystals. *J. Appl. Phys.* **98** 064101 (2005).
- [25] Choi, K. J. et al. Enhancement of ferroelectricity in strained BaTiO₃ thin films. *Science* **306**, 1005 (2004).
- [26] Pertsev N.A., Tagantsev A.K., Setter N. Phase transitions and strain-induced ferroelectricity in SrTiO₃ epitaxial thin films *Phys. Rev. B* **61** R825 (2000).
- [27] Zubko, P. et al. Electrostatic Coupling and Local Structural Distortions at Interfaces in Ferroelectric/Paraelectric Superlattices. *Nano. Lett.* **12** 2846 (2012).
- [28] Brooks, C.M., et al. Growth of homoepitaxial SrTiO₃ thin films by molecular-beam epitaxy. *Appl. Phys. Lett.* **94** 162905 (2009).
- [29] Dawber, M. et al. Tailoring the properties of artificially layered ferroelectric superlattices. *Adv. Mater.* **19** 4153 (2007).
- [30] Aguado-Puente, P. & Junquera, J. Structural and energetic properties of domains in PbTiO₃/SrTiO₃ superlattices from first principles, *Phys. Rev. B* **85** 184105 (2012).

- [31] Kittel, C. Theory of the structure of ferromagnetic domains in films and small particles. *Phys. Rev.* **70** 956 (1946).
- [32] Lisenkov S., Ponomareva I. & Bellaiche L. Unusual static and dynamical characteristics of domain evolution in ferroelectric superlattices. *Phys. Rev. B* **79** 024101 (2009).
- [33] Zubko, P. , Stucki, N., Lichtensteiger, C., & Triscone, J.-M. X-Ray Diffraction Studies of 180 degrees Ferroelectric Domains in $\text{PbTiO}_3/\text{SrTiO}_3$ Superlattices under an Applied Electric Field, *Phys. Rev. Lett.* **104**, 187601 (2010).
- [34] Jo, J.Y., et al. Nanosecond Dynamics of Ferroelectric/Dielectric Superlattices. *Phys. Rev. Lett* **107** 055501 (2011).
- [35] Chen, P. et al. Field-Dependent Domain Distortion and Interlayer Polarization Distribution in $\text{PbTiO}_3/\text{SrTiO}_3$ Superlattices *Phys. Rev. Lett* **110** 047601 (2013).
- [36] Paruch, P. and Triscone, J.-M. High-temperature ferroelectric domain stability in epitaxial $\text{PbZr}_{0.2}\text{Ti}_{0.8}\text{O}_3$ thin films. *Appl. Phys. Lett* **88** 162907 (2006).
- [37] Paruch, P., Koltun, A.B., Hong, X., Ahn, C.H., & Giamarchi T. Thermal quench effects on ferroelectric domain walls. *Phys. Rev. B* **85** 214115 (2012).
- [38] Kalinin, S.V. & Bonnell, D.A. Effect of phase transition on the surface potential of the BaTiO_3 (100) surface by variable temperature scanning surface potential microscopy. *J. Appl. Phys* **87** 3950 (2000).
- [39] Kalinin, S.V. and Bonnell, D.A. Temperature dependence of polarization and charge dynamics on the $\text{BaTiO}_3(100)$ surface by scanning probe microscopy. *Appl. Phys. Lett.* **78** 1116 (2001).
- [40] McGilly, L.J., Burnett, T.L., Schilling, A., Gain, M.G. & Gregg, J.M. Domain annihilation due to temperature and thickness gradients in single-crystal BaTiO_3 . *Phys. Rev. B* **85** 054113 (2012).
- [41] Catalan, G., Seidel, J., Ramesh, R. & Scott, J.F. Domain wall nanoelectronics. *Rev. Mod. Phys* **84** 119 (2012).

SUPPLEMENTARY INFORMATION FOR “RAPID IN-SITU X-RAY DIFFRACTION DURING THE GROWTH OF FERROELECTRIC SUPERLATTICES” BY B. BEIN ET AL.

A. Growth rates

From the reflectivity data we can extract the growth rates per unit cell for STO grown on STO as (66.6 ± 2.0) s/unit cell, BTO grown on STO as (43.3 ± 1.3) s/unit cell for the first four layers and increasing after that. Within the BTO/STO superlattice the BTO growth rate is (44.5 ± 3.6) s/unit cell which is the same as for BTO on STO. The average growth rate for STO within the superlattice is not the same as when it is grown directly on STO. The measured average growth rate is (74.2 ± 7.6) s/unit cell, but a closer inspection reveals that the growth rate is different for odd unit cells, which take (80.2 ± 5.7) s/unit cell to complete and even unit cells which take (68.2 ± 3.2) s/unit cell. We believe that this is caused by the STO in the superlattice growing with a SrO termination (coming from growing on BaO terminated BTO surfaces), in contrast to the TiO₂ termination it normally has when growing directly on the substrate.

B. Scan calculations

To better illustrate the used scanning method we calculated the h,k and l values for the detector area during the rocking of the θ motor. Fig. S1 (a) shows the difference in h between the first and the last angle of the scan. One can see that the h value for each pixel of the detector does not change during the scan. The same is true for the l values of each pixel (see Fig. S1 (c)). The only direction in which one integrates during this kind of scan is the k direction. This is shown in Fig. S1 (b). During the scan each pixel integrates over the k values between the first and last plane. This corresponds to a vertical line in the k direction in Fig. S1 (b).

C. Surface termination

The CTR of the (001) peak depends strongly on the surface termination of the heterostructure(see Fig. S2). We demonstrate this with the examples of the first bilayer of a

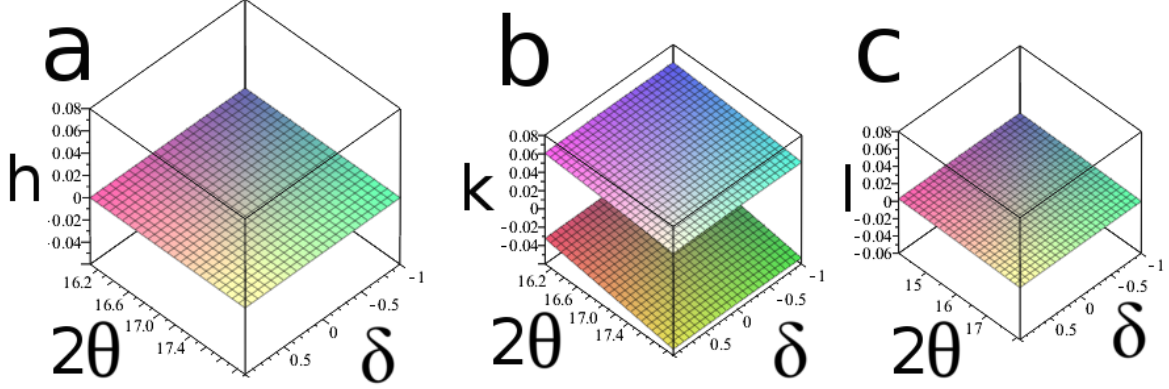


FIG. S1. (a) Difference in h between the first and the last angle of the motion in θ . (b) k values for the first and the last angle of the motion in θ . (c) difference in l between the first and the last angle of the motion in θ . In panel (a) and (c) we show that the l and h values of the detector do not change during the rocking of the sample. In panel (b) we have two different planes for the first and last scan. The detector integrates over the volume between the planes during the scan.

2/6 BTO/STO superlattice grown on STO. This heterostructure contains 6 unit cells STO on top of 2 unit cells BTO and is grown on a STO substrate. There are two possible surface terminations for this example. One is the TiO_2 surface termination, which is the expected surface termination of the substrate after chemical treatment. The other one is SrO surface termination. Our fit for the SrO surface termination for the superlattice and TiO_2 termination (red), SrO termination (orange) of the substrate is shown in Fig. S2 (a). One can see that these are good fits to the measured data but one can not distinguish between the two substrate surface terminations. The superlattice is fitted with an average out of plane lattice parameter of 3.99\AA . When we simulated the same superlattice (with the same average out of plane lattice parameter of 3.99\AA) with a TiO_2 surface termination of the superlattice and TiO_2 termination (blue), SrO termination (cyan) of the substrate Fig. S2 (b), we could not observe a good match with the taken data. Finally we tried to fit the superlattice with a TiO_2 surface termination of the superlattice and TiO_2 termination (blue), SrO termination (dark blue) of the substrate Fig. S2 (c). These fits lead to an average out of plane lattice parameter of 3.86\AA , which is smaller than the lattice parameters of STO and BTO and makes this fit unrealistic. This leads to the conclusion that the superlattice has a SrO surface termination after the first bilayer. By changing the growth parameters one

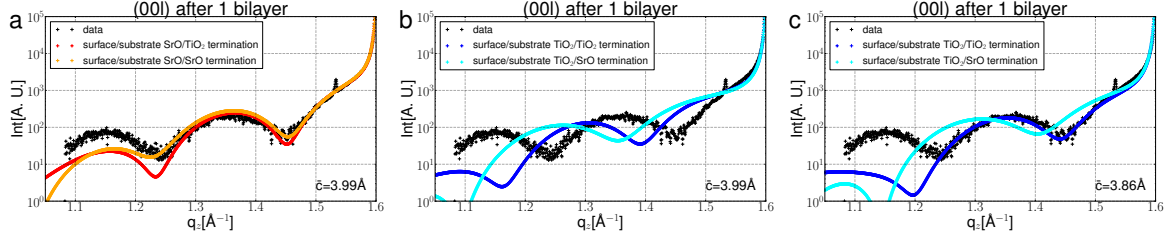


FIG. S2. The figure shows the data(black) of the 2/6 BTO/STO on STO superlattice after the growth of one bilayer. (a) shows fits for a SrO surface termination of the superlattice and TiO₂ termination(red), SrO termination(orange) of the substrate, the superlattice is fitted with an average out of plane lattice parameter of 3.99Å. One can see that these are good fits to the measured data but one can not distinguish between the two substrate surface terminations. (b) shows fits for a TiO₂ surface termination of the superlattice and TiO₂ termination(blue), SrO termination(cyan) of the substrate, the superlattice is fitted with an average out of plane lattice parameter of 3.99Å. These fits don't fit the data well. (c) shows fits for a TiO₂ surface termination of the superlattice and TiO₂ termination(blue), SrO termination(cyan) of the substrate, the superlattice is fitted with an average out of plane lattice parameter of 3.86Å. The blue fit is good but the average out of plane lattice parameter is smaller than the lattice parameters of STO and BTO which makes this fit unrealistic.

might be able to change the surface termination.

D. Piezo Force Microscopy

To show that the samples are ferroelectric at room temperature Piezo Force Microscopy (PFM) was performed on the samples with a SRO back electrode. First a square pattern domain was written onto the sample by applying a constant bias of 5V to the sample in the square area. Afterwards the domains were read out using Dual AC Resonance Tracking(DART) PFM. The experiment was performed on an Asylum MFP3D Atomic Force Microscope(AFM). Fig. S3 shows the taken data panels (a1), (b1), (c1) are for the 2/6 BTO/STO sample and panels (a2), (b2), (c2) are for the 1/7 BTO/STO sample. The phase 1 signal is shown in Fig. S3 (a1), (a2). The areas of the sample which are polarized in different directions show a clear phase shift. One can observe the phase shift for the phase

2 signal in Fig. S3 (b1), (b2), where the high and low phase signal between the domains switched. This shows the correct tuning of the instrument. Fig. S3 (c1), (c2) show point PFM measurements, one can see the phase hysteresis and butterfly loops in the piezoelectric response.

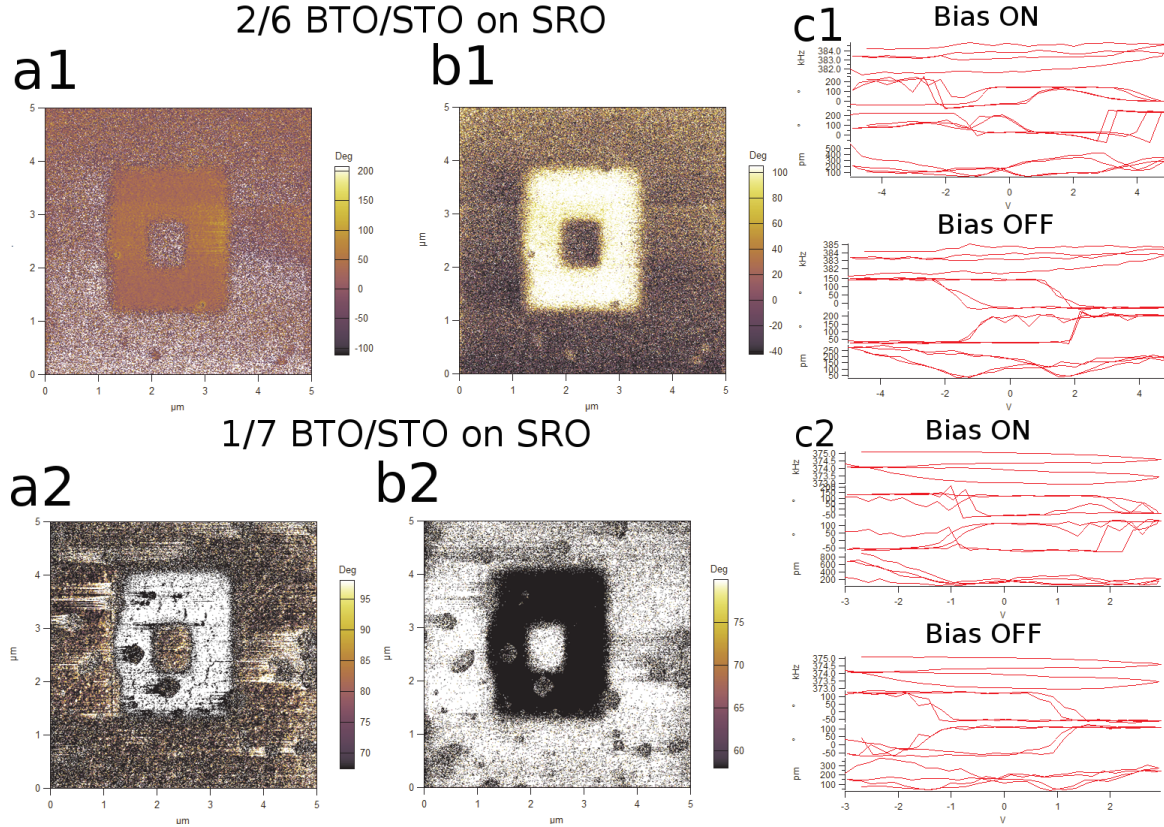


FIG. S3. The top panels (a1), (b1), (c1) show PFM data for the 2/6 BTO/STO grown on SRO sample. The bottom panels (a2), (b2), (c2) show PFM data for the 1/7 BTO/STO grown on SRO sample. (a1), (a2) Phase 1 data, (b1), (b2) Phase 2 data taken with DART PFM. The data was taken after writing the square with a constant bias into the superlattices. (c1), (c2) point PFM measurements one can see the phase hysteresis and butterfly loops in the piezoelectric response. Both show that the measured samples are ferroelectric at room temperature.

E. Movies

We have prepared several movie files from the experiments which will be available with the published version of this paper. Readers from the arxiv who are interested in seeing

these movies should contact the corresponding author.

- `2_6_data_17fps.mov`

As an example of the raw data we have converted the Pilatus camera images acquired during the growth of the 2/6 sample on STO in to a continuous movie. Each frame corresponds to a 20 second exposure and the framerate of the movie is 17fps, so the movies are considerably sped up from the real time experiment. The resolution of the image is also considerably reduced from what was used for analysis to meet journal limitations. In addition to the camera image we have included the two principle line scans from which data was extracted and the average out of plane lattice parameter and domain size as an evolving plot.

- `001_2_6_onSTO.mov`, `001_2_6_onSRO.mov`,
`001_1_7_onSTO.mov`, `001_1_7_onSRO.mov`

These movies show the evolution of the 001 scans and the fits to each scan on each of the 4 principle samples studied.

- `2_6_domains_STO_fit_lin.mov`, `2_6_domains_SRO_fit_lin.mov`,
`1_7_domains_STO_fit_lin.mov`, `1_7_domains_SRO_fit_lin.mov`

These movies show the evolution of the diffuse scattering associated with polarization domains along with two fitting approaches that were tried.

Fit lin means that the least square minimization used was: $(fit(Q_x) - data(Q_x))^2$

Fit log means that the least square minimization used was: $(\log_{10}(fit(Q_x)) - \log_{10}(data(Q_x)))^2$

The analysis presented in the paper is based on the linear least square minimisation, Fit lin.